

# A High-Fidelity Study of High-Pressure Diesel Injection

Marco Arienti

Sandia National Laboratories

Mark Sussman

Florida State University

Copyright © 2015 SAE Japan and Copyright © 2015 SAE International

## ABSTRACT

A study of n-dodecane atomization, following the prescribed unseating of the needle tip, is presented for a high-pressure, non-cavitating Bosch Diesel injector ("Spray A", in the Engine Combustion Network denomination). In the two simulations discussed here, the internal and external multiphase flows are seamlessly calculated across the injection orifice using an interface-capturing approach (for the liquid fuel surface) together with an embedded boundary formulation (for the injector's walls). This setting makes it possible to directly relate the liquid jet spray characteristics (under the assumption of sub-critical flow and with a grid resolution of 3  $\mu\text{m}$ , or 1/30 of the orifice diameter) to the moving internal geometry of the injector. Another novelty is the capability of modeling the compressibility of the liquid and the gas phase while maintaining a sharp interface between the two. With an equation of state calibrated for n-dodecane, we briefly examine the difference in exit jet characteristics for adiabatic and isothermal wall conditions.

## INTRODUCTION

While the specific atomization process of liquid fuel is often crucial in determining the fuel vapor-air mixture, which in turn controls performance and emissions, spray model inadequacies are presently a major barrier. Progress could be achieved by accurately characterizing the flow immediately outside of the injector's orifice, therefore setting the correct boundary conditions for turbulent combustion in the engine cylinder. However, the measurement of key model information, such as the rate of injection (ROI) and rate of momentum (ROM) of the jet, are affected by various factors. For instance, Pickett et al. (2013) have reported a lack of consistency in measurements taken during the early startup injection period. Flow rate measurements are further complicated by the expansion of the jet both inside and outside the orifice. This, coupled to the thermal conditions at the wall, can lead to non-trivial variations of temperature and density of the injected fuel. And, as we will see, small deviations from the nominal geometry of the orifice

can modify the flow in the sac and introduce further variability in the measurement. Efforts by the Engine Combustion Network (ECN) to characterize a specific set of injectors at given operational conditions have brought together modelers and experimentalists in the attempt to solve these issues.

The results presented here are focused on the role of the aforementioned non-idealities in modeling the ROI and ROM at high injection pressure for a well-defined injection device. We carry out a time-resolved simulation of the gas-liquid interface inside and outside of the injector in the early transient phase of injection: assuming that all the physical processes are correctly resolved on the computational grid, no other model is introduced in the simulation.

An example of this high-fidelity approach is the massive simulation of a liquid jet by Shinjo and Umemura (2011). That study only concerned the external flow with respect to the injector, with injection velocities of the order of 100 m/s or less, whereas we consider the complete geometry of the injector tip and reach exit jet velocities that are five or six times larger. A similarly broad range of flow velocities was considered in a recent study by Bode et al. (2014), but in the incompressible limit. That work included the injector geometry in a parametric study of the orifice taper ratio, but used an all-open needle configuration and was limited to the first 3 microseconds of injection. The complete injection period was instead covered by Xue et al. (2013) in a comparison of the mass flow rate resulting from the needle's movement with or without wobble: the liquid phase was treated as incompressible while the gas phase was compressible. However, those calculations were carried out only inside the injector and in the context of the Reynolds-Averaged Navier-Stokes (RANS) formulation (albeit with a respectable 7.5  $\mu\text{m}$  of minimum grid spacing). Additional references on fuel injection studies can be found in the three aforementioned papers.

The approach discussed here does not include a turbulent model, as we felt that none has been proven so far to correctly capture the dynamics of the gas-liquid interface: we will later examine the consequences of this choice. A novel element in this study is that the setup is customized to a specific

injector from Robert Bosch LLC, specimen 210675, by including some of the injector's asymmetries as they are reported in the ECN data archive. We also exactly implement the time-dependent needle motion during the initial part of the injection cycle. The simulation covers the first 370  $\mu$ s from needle activation, including the 35  $\mu$ s that follow the appearance of the liquid from the orifice exit. Although the results will be mostly discussed with respect to a baseline simulation with adiabatic wall boundary conditions, a second case with fixed wall temperature will be shown for comparison.

## NUMERICAL METHOD

This section synthesizes recent work on compressible, multiphase flow for high-pressure fuel injection, including the time-varying geometry of the injector and a realistic equation of state for n-dodecane.

The liquid-gas interface is captured by the ELVIRA method (Pilliod and Puckett, 2004), except for the contact lines at the solid boundary, which are treated by the coupled level-set moment-of-fluid (CLSMOF) method (Jamison et al., 2013). In the CLSMOF algorithm, a piecewise-linear interface reconstruction uses information from the level-set function, the volume-of-fluid function and the phase centroid of the computational cell to produce a slope and an intercept for the local reconstruction of the gas-liquid interface. The extra information on the phase centroid enables the correct partition of multi-material computational cells at a contact line.

The level-set function is maintained at each time step as the signed distance to the reconstructed interface. The curvature is evaluated from the level set function by using the method of heights (Sussman and Ohta, 2009). The two-phase compressible Navier-Stokes equations are solved with a new mass-, momentum-, and energy-conserving advection algorithm.

A new semi-implicit pressure update scheme asymptotically preserves the standard incompressible pressure projection in the limit of infinite sound speed (Jemison et al., 2014). This attribute makes the new method applicable to compressible flows, including liquids with stiff equations of state, while using time steps that can be larger compared to typical explicit methods.

The injector wall boundaries are represented by the embedded boundary method described by Arienti and Sussman (2014). The embedded boundary method uses one more signed distance function, the "solid" level set: its magnitude is the minimal distance between the regular cell center and the surface of the body, and, by convention, the sign is positive outside the body and negative inside it. When applied to the motion of solid interfaces, the embedded boundary sweeps the computational Cartesian cells in a robust manner: contact and separation of boundaries, such as during the unseating of the needle, occur in a very straightforward manner.

Another component of our simulation capability is the use of block-structured, adaptive mesh refinement (AMR). The coarsest level (the base level) is denoted as level zero and is a Cartesian box covering the whole simulation domain, including part or all of the solid body. Cell tagging targets the gas-liquid interface

and possibly the solid interface, or special features of the flow (shocks, for instance), to form level one. The new level can in turn be tagged for refinement, and the process is repeated until the input grid resolution is achieved. The refinement ratio between two consecutive levels is two. A minimum number of cells on any block side defines the granularity of the AMR simulation: this blocking factor is 32 in this work. At each re-gridding operation, new grids are combined to cover all the tagged cells within the assigned coverage efficiency. Data on the fine level are either copied from a previous time step or, when the grid structure has changed locally, they are conservatively interpolated from the underlying coarse level. The liquid-gas interface is always embedded in the finest grid level to avoid gross interpolation errors from the calculation of the fluxes of mass, momentum and energy across fine-coarse boundaries. An extensive discussion on this topic can be found in Kadiouglu and Sussman (2008).

The definitions and operators necessary to carry out the AMR tasks are provided by the BoxLib library (CCSE 2012), which is developed and maintained by the Center for Computational Sciences and Engineering group at Lawrence Berkeley National Laboratories. In a parallel simulation, BoxLib attempts to manage the grid blocks in order to optimize the distribution of computational load amongst all the available processors.

## INJECTOR MODEL

### INJECTOR PROPERTIES

Spray A is a Bosch injector of 90  $\mu$ m nominal diameter at the orifice exit. As with all the other injectors of this batch, the SN 210675 specimen is affected by slight manufacturing defects that affect the orifice alignment with the injector axis, its cross-section and tapering: the reader is referred to the ECN web site for full documentation. We chose to reproduce the measured off-center position of the orifice axis with respect to the sac: 53  $\mu$ m at  $\theta = +9^\circ$  in the convention of Figure 1. This offset means that the inlet-turning angle is lower on one side of the orifice compared to the opposite side.

The walls of the Diesel injector are the only elements of the solid body that need to be discretized to carry out the simulation on the set Cartesian boxes. The wall tessellation is read at the beginning of the simulation as a list of node coordinates and of node sequences forming every face. To simulate the unseating of the needle, the injector is divided in two parts, the needle tip and the cap, as displayed in Figure 2. The rigid translation of the needle with respect to the injector cap follows an assigned trajectory. In frame (a) the needle's base is almost completely inside the computational domain (marked by a dashed line), whereas in its fully open position in frame (c) the base of the needle has moved outside. Frame (b) shows an intermediate position and the effect of the deviation from a perfectly axial trajectory: the annular fuel passage is obviously asymmetric at this time.

The trajectory of the needle, discussed in Kastengren et al. (2012), is shown in Figure 3 for the X- Y- and Z-

components (continuous, dashed and dotted line, respectively). Time zero corresponds to the instant when the injection command is given: the same reference time is used in our simulations. The overall recorded time that is available from the ECN archive is 5000  $\mu$ s, but the needle does not actually move for the first 160  $\mu$ s. Substantial lateral displacements in addition to the nominal axial motion can be observed in Figure 3. The peak needle lift is reached after approximately 900  $\mu$ s, then the needle reverses direction and closes at approximately 1800  $\mu$ s. The corresponding needle velocity is of the order of one meter per second or less. The simulation will only cover the early transient of the needle unseating, corresponding to the first 370  $\mu$ s from needle activation.

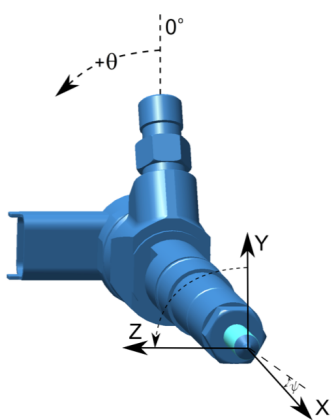


**Figure 1. Spray A and reference coordinates.**

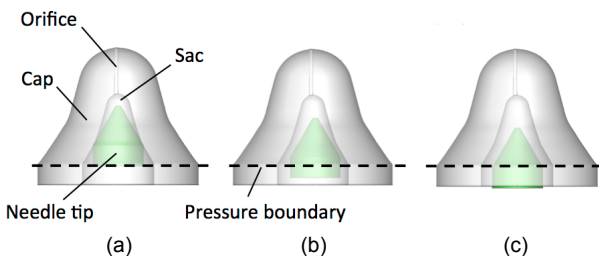


**Figure 2. Sequence illustrating the relative motion of the needle tip with respect to the cap. The dashed line is the trace of the boundary plane of the computational domain.**

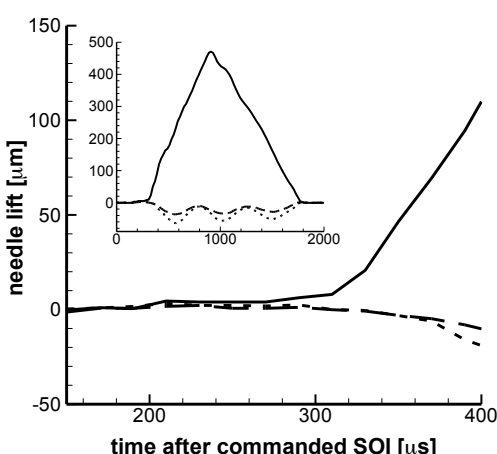


**Figure 3. Trajectory of the needle with respect to the cap. The insert shows the complete trajectory of the needle, in the same units.**

## PHASE PROPERTIES

The liquid and gas phase properties are evaluated at run-time as a function of pressure, phase density and phase internal energy. The surface tension coefficient for n-dodecane in air is kept constant at 0.024 N/m and the static contact angle on the injector's wall is 90°. The thermal conductivities are also constant: for air,  $k = 0.026 \text{ W/m}\cdot\text{K}$ ; for n-dodecane,  $k = 0.157 \text{ W/m}\cdot\text{K}$ .

The gas phase is calculated as a perfect gas with the properties of air. The liquid phase is calculated via a set of correlations derived from high-pressure measurements, as explained below.

### Equation of state of n-dodecane

The liquid phase pressure,  $P(\rho, T)$ , is calculated using the Tait formulation with the coefficients proposed by Caudwell et al., (2004) for pressures up to 200 MPa in the temperature range 298–473 K:

$$\rho = \frac{\rho_0}{1 - A \ln[(B + P)/(B + P_0)]}$$

with  $A = 0.08998$ . The pressure is expressed in MPa, the density in  $\text{kg}\cdot\text{m}^{-3}$ , and temperature in degrees Kelvin.  $B$  depends only on temperature,

$$B = \sum_{i=0}^2 b_i T^i,$$

with  $b_0 = 345.1$ ,  $b_1 = -1.1458 \text{ K}^{-1}$ ,  $b_2 = 0.9837 \cdot 10^{-3} \text{ K}^{-2}$ . The reference density at  $P_0 = 0.1 \text{ MPa}$  is

$$\rho_0 = 921.1984 - 0.47516 T - 3.922 \cdot 10^{-4} T^2.$$

As a correlation for internal energy was not immediately available, an expression for  $e(P, T)$  was derived by the authors. The correlation is

$$e(P, T) = \sum_{i=0}^4 g_i(P) T^i,$$

with

$$g_0 = 19.94245;$$

$$g_1 = 2.273845 + 7.701613 \cdot 10^{-6} P(P - P_0);$$

$$g_2 = -2.279889 \cdot 10^{-3} - 3.654273 \cdot 10^{-4} P;$$

$$g_3 = 6.106366 \cdot 10^{-6};$$

$$g_4 = -3.266302 \cdot 10^{-9}.$$

The dependence on  $P$  in  $g_1$  and  $g_2$  is justified in view of the thermodynamic relation

$$\left( \frac{\partial e}{\partial P} \right)_T = \frac{1}{\rho} (\beta_T P - \alpha_P T)$$

that is used for evaluating

$$e(P, T) \approx e(P_0, T) + (P - P_0) \left( \frac{\partial e}{\partial P} \right)_T$$

in the fitting procedure. The isothermal compressibility (in MPa<sup>-1</sup>),  $\alpha_P$ , and the isobaric expansion coefficient (in K<sup>-1</sup>),  $\beta_T$ , are the values tabulated in the range from 0.1 to 140 MPa and from 293.15 to 433.15 K by Khasanshin et al. (2003).

Finally, the inverse problem of finding temperature from known internal energy and density,  $T(e, \rho)$ , is solved via an iterative method.

### Speed of sound

The speed of sound in the liquid phase is calculated from a separate function of temperature and pressure,

$$\frac{c - c_0}{c} = D \ln \left[ \frac{E + P}{E + P_0} \right],$$

where the reference atmospheric speed of sound is

$$c_0 = 4094 - 183.21 T^{0.5} + 0.07974 T^{1.5} - 2.348 \cdot 10^{-6} T^3.$$

The coefficients  $D$  and  $A$  are a function of temperature, pressure and carbon number of the fuel (Padilla-Victoria et al., 2013). For pure n-dodecane,

$$D = 0.1652 + 2.5 \cdot 10^{-3} T - 5.85 \cdot 10^{-6} T \cdot P;$$

$$E = -56.91 + 7.3674 \cdot 10^{-5} T^2 + 0.02260 T + 463.5 \cdot \exp(-0.001687 T).$$

The correlation for  $D$  was modified by the authors, with respect to the one proposed by Padilla-Victoria et al., (2013) to obtain a better match with the values reported by Khasanshin et al. (2003) in the temperature range 293-433 K and for pressures between 0.1 to 140 MPa.

### Dynamic viscosity

The dynamic viscosity  $\mu(\rho, T)$  is calculated in the range from 298.15 and 473.15 K and at pressures up to 200 MPa using the correlation by Caudwell et al. (2004):

$$\mu / (\text{Pa} \cdot \text{s}) = \mu^* \cdot [4.778 \cdot 10^{-9} V^{-2/3} M^{1/2} T^{1/2}].$$

where  $V$  is the molar volume in m<sup>3</sup>·mol<sup>-1</sup> and  $M$  is the molar mass in kg·mol<sup>-1</sup>. The coefficient  $\mu^*$  is a dimensionless viscosity

$$\frac{1}{\mu^*} = \sum_{i=0}^3 d_i (V/V_0)^i.$$

For n-dodecane, the coefficients  $d_i$  are:  $d_0 = 0.321621$ ;  $d_1 = -0.4803715$ ;  $d_2 = 0.222206$ ;  $d_3 = -2.9964626 \cdot 10^{-2}$ .  $V_0$  is a temperature-dependent molar core volume given by

$$V_0 = 10^{-6} \sum_{i=0}^3 f_i T^i.$$

The coefficients  $f_i$  are:  $f_0 = 191.54$ ;  $f_1 = -0.441338 \text{ K}^{-1}$ ;  $f_2 = 8.98744 \cdot 10^{-4} \text{ K}^{-2}$ ;  $f_3 = -6.7792 \cdot 10^{-7} \text{ K}^{-3}$ .

We note that the dependence of dynamic viscosity on pressure cannot be ignored. The smallest dynamic

viscosity tabulated by Caudwell et al. (2004) is 0.218 mPa·s at 0.1 MPa and  $T = 473.15$  K; the largest value is 5.728 mPa·s at 152.18 MPa and 298.15 K. As an example, taking the tabulated values at 0.1 MPa and 293.15 K ( $\rho = 746 \text{ kg/m}^3$  and  $\mu = 1.344 \text{ mPa} \cdot \text{s}$ ), and assuming a fuel exit velocity of 600 m/s, the Reynolds number based on the orifice diameter is  $Re = 30,000$ . At the same temperature, but at 152 MPa, the dynamic viscosity is larger by more than a factor of four,  $\mu = 5.728 \text{ mPa} \cdot \text{s}$ , while the density increases only by 10%, bringing the Reynolds number down to 7,700.

### SIMULATION SETUP

Calculations were carried out on the Redsky Sandia cluster by using, on average, 128 SUN X6275 blades (2.93 GHz dual socket/quad core configuration with 12 GB RAM per blade) for a total of 512 cores. The latest stages of the simulation required 256 blades, or 1024 cores. The base computational domain is a regular Cartesian 64×64×576 box with the longest side, oriented along the injector's axis, of length 1.53 cm (170 times the exit orifice diameter). This size is substantially longer than in similar high-fidelity simulations because we intend to follow the jet penetration for a sufficient time period. Three levels of refinement are added to the coarse level in order to obtain a minimum grid spacing of 3.32 μm, corresponding to 27 computational cells across the orifice diameter. At this grid resolution, a stable time step for the flow of interest (with a supersonic transient in the gas phase) is of the order of a nanosecond. Because of the spray development, the total count of cells increases during course of the simulation. As the fuel makes its way through the orifice and then outside of the injector, this number steadily climbs from approximately  $7 \cdot 10^7$  to  $21 \cdot 10^7$ . Still, such a cell count corresponds to a rather coarse representation of the liquid-phase turbulence. An order of magnitude increase in grid resolution was achieved with  $6 \cdot 10^9$  cells in an external flow simulation by Shinjo and Umemura (2011).

The typical edge length of the injector's tessellation is of the order of one or two micrometers where the wall curvature is the largest. The auxiliary grid for the solid level set (described by Arienti and Sussman, 2014) has constant spacing of 9 μm. The wall boundary velocities that are necessary to populate the ghost region of the solid are calculated directly by differentiation of the displacement values read from the trajectory file.

The fixed injection pressure of 150 MPa is applied directly as a constant value at the boundary face, as shown Figure 2. While this is a convenient simplification – fluctuations of up to 8 MPa have been reported in Pickett et al. (2013) – it is also acceptable for the simulation interval considered here (future studies will include injection pressure variability as well). A fixed exit pressure of 2 MPa is applied to the other five sides of the computational domain box.

The initial temperature of the liquid is uniformly 343 K in both the reservoir and the cap. The initial temperature of the gas is 303 K. This is not the reference 900 K temperature prescribed for Spray A, but corresponds to the non-evaporating condition

used for radiographic measurements of fuel mass at Argonne (Pickett et al., 2014). In the isothermal wall simulation the wall temperature is  $T_w = 393$  K.

## RESULTS

### INTERNAL FLOW

The simulation begins with a partially liquid-filled sac. The volume left to the gas is  $0.065 \text{ mm}^3$ , or approximately one third of the sac volume. The volume of the cylindrical orifice, of nominal diameter  $90 \mu\text{m}$ , is much smaller,  $0.006 \text{ mm}^3$ . A partially filled sac setup is motivated by the observation (via long-distance microscopy and high-contrast display) that a gas or vapor jet is ejected from the orifice before the liquid (Pickett et al., 2013). For the same injection configuration that is studied here, the ejection was reported to take place approximately  $7 \mu\text{s}$  before the exit of the fuel from the orifice, suggesting that a certain amount of gas or vapor is already in the sac prior to injection.

A sequence related to the first part of the needle lifting is displayed in Figure 4, where time is counted from the activation of the needle. The simulation indicates that gas from outside the injector is actually sucked in, from approximately  $t = 173 \mu\text{s}$  to  $180 \mu\text{s}$  from the start of commanded injection (SOI). This short-duration flow is due to the receding motion of the needle's tip while the sac is still sealed off from the fuel reservoir: the tip motion is almost imperceptible in this time interval, but the volume displacement is sufficient to cause suction. Thus, at time  $t = 235.5 \mu\text{s}$ , the inverted gas jet can be seen to affect the free surface of the fuel.

The obstruction to new liquid entering the cavity begins to be removed a few tens of microseconds later, as the needle begins to lift. This is shown in Figure 4 at  $t = 315.5 \mu\text{s}$  by the sudden velocity increase at the bottom of the domain. Note that gaps are still not visible in the  $Z = 0$  cross-section because, as noted before, the lifting of the tip is not axis-symmetrical. The injection process is in fact interrupted a few microseconds later because of the wobbling motion of the needle that causes the free surface to slightly oscillate: it is only by  $t = 330 \mu\text{s}$  that the fuel passage completely opens and fuel injection begins. In describing this process it is also noted (see Figure 3) that in the first  $300 \mu\text{s}$  the needle's motion is within less than  $5 \mu\text{m}$  and that the minimum grid resolution is only  $3.32 \mu\text{m}$ .

Once the needle tip is sufficiently removed from the cap's walls, the liquid begins to fill the sac very rapidly. Two main phenomena can be observed at this stage. The first is the asymmetric filling of the orifice that leaves a small pocket of trapped gas at the orifice inlet, as shown by Figure 6. This occurrence can be tracked back to the out-of-axis position of the orifice with respect to the injector. Several smaller bubbles can also be observed. The volume occupied by the residual gas is a small percentage of the initial gas volume, approximately  $3 \cdot 10^{-4} \text{ mm}^3$ , or 0.15% of the sac volume. The bubble is eventually compressed and expelled later on.

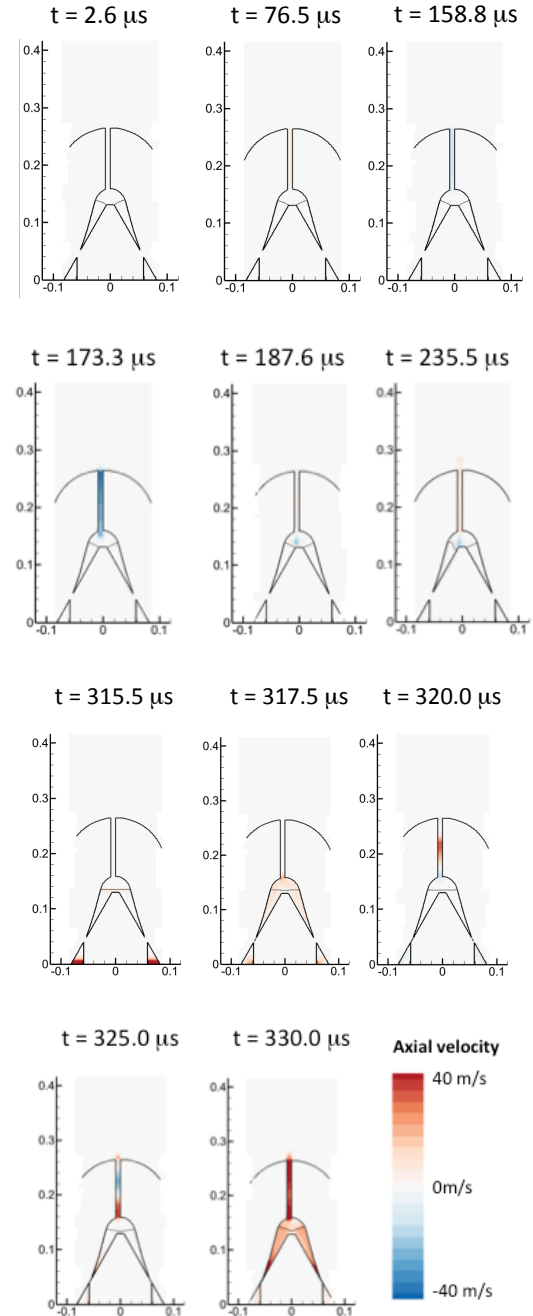


**Figure 4. Axial velocity of the gas and liquid phase in the early opening transient as captured by the  $Z = 0$  cross-section of the domain. In the cross-section, the thicker continuous line corresponds to the boundaries of the needle and the orifice, while the thinner line represents the free surface of the liquid.**

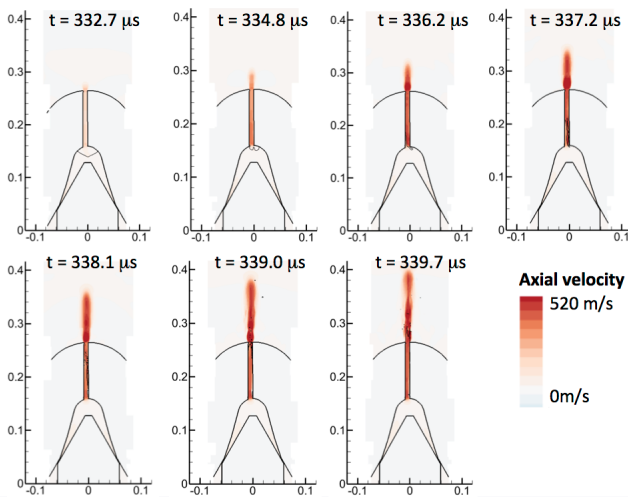


**Figure 5.** This is a continuation of Figure 4 and follows the same drawing conventions. Note the increase of axial velocity by a factor of 10 with respect to the previous injection interval.

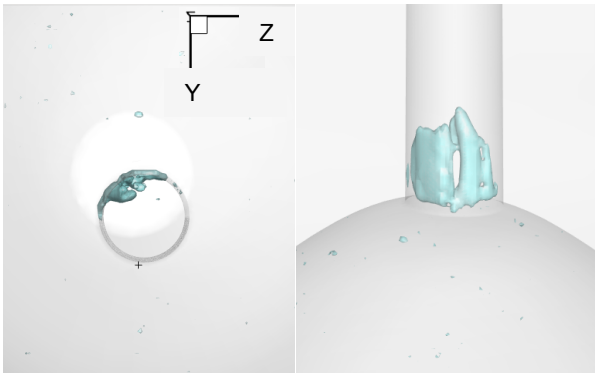


**Figure 6.** Front and side view of gas bubble at 339  $\mu$ s.

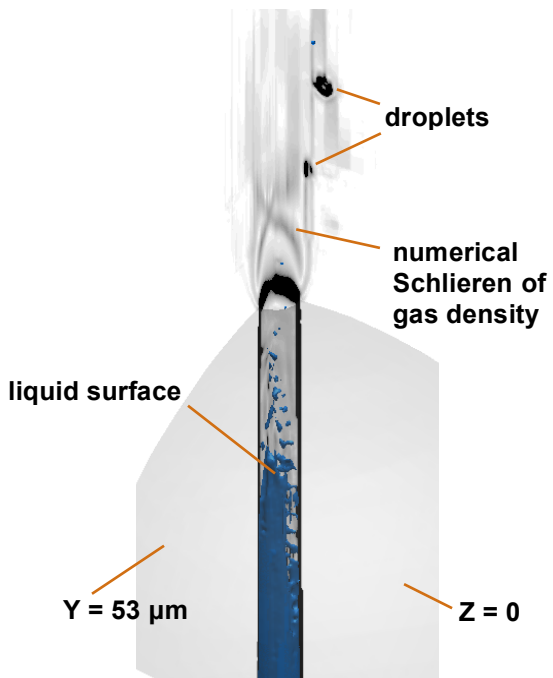


**Figure 7.** Detail of under-expanded jet in the gas phase (numerical Schlieren) at  $t = 337.2 \mu$ s. The two orthogonal slices cross at the axis of the orifice. Also shown is the volume rendering of the liquid surface at the same time.

The second phenomenon is that, as soon as the gas is pushed outside of the orifice, it reaches supersonic conditions that persist until the orifice volume is replaced by fuel. At time  $t = 337.2 \mu$ s, the gas has reached a Mach number of 1.2 at the orifice exit and it is expanding outside the injector above Mach two. Approximately two orifice diameters downstream of the injector's exit, pressure has decreased along the axial direction to 0.057 MPa. Features of the under-expanded jet and the accompanying barrel shock (with axial compression ratio of 4.5) can be observed within two diameters from the orifice exit after 336  $\mu$ s in Figure 7. The barrel shock disappears four microseconds later when the liquid fuel fills the orifice.

The fuel emerges from the orifice at 340  $\mu$ s. This delay with respect to the SOI depends on the amount of residual gas volume inside the sac, and can be expected to vary between injection cycles. At the time shown in Figure 8, the liquid in the sac has reached the inlet pressure value. Resistance to the flow is mostly offered by the constriction at the orifice entrance: after passing the gap between the needle and the sac walls, the fuel is actually compressed above the inlet value of 150 MPa until it reaches the orifice entrance. There, the pressure abruptly decreases to 80 MPa and inside the orifice it further equilibrates to the external pressure.

As shown in Figure 8, left column, for the case of adiabatic walls, the fuel density after passing the gap is slightly larger than in the reservoir; it decreases as the passage width increases toward the sac, but then grows again and finally reaches a maximum value of more than 790 kg/m<sup>3</sup>. Along the same path, the temperature has variations of opposite sign with respect to density, and reaches 360 K in the sac. The exit temperature eventually returns to 346 K (averaged at the orifice cross-section), very close to the inlet value. The average density at the orifice exit is instead 716 kg/m<sup>3</sup>, substantially below the inlet value. Temperature, pressure and density eventually all decrease in the external jet.

An asymmetry in temperature distribution can be observed along the orifice, with what appears as a hotter boundary layer on the right-hand side of the orifice's wall. This side is where the flow is slowed down by the sharper turning angle upstream. Since the walls are adiabatic, we speculate that the original increase in temperature is due to heat transfer from a collapsing gas bubble, shown a few microseconds earlier in Figure 6 (further investigation is required on this point).

A similar trend, with slightly larger temperatures, can be observed in the second simulation run with isothermal walls at  $T_w = 383$  K. The time in the snapshot of Figure 8, right column, is  $t = 352 \mu$ s. The temperature at the orifice exit is on average 361 K in this case, 15 K more than in the adiabatic case, while the density is almost the same, 713 kg/m<sup>3</sup>. The thermal boundary layer on the left-hand side of the orifice is now thicker than in the adiabatic simulation.

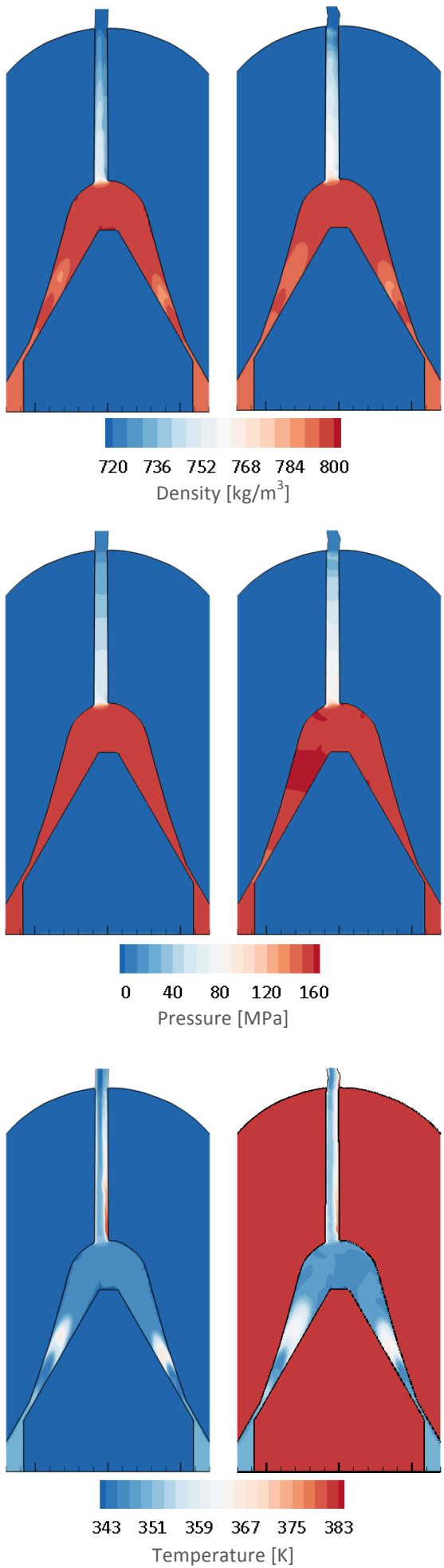


**Figure 8. Distribution of density, pressure and temperature at the  $Z = 0$  cross-section (gas phase)**

not shown). Two cases are compared at almost the same time from SOI. Left: adiabatic injector walls (baseline case) at  $t = 354 \mu\text{s}$ . Right: injector walls at fixed  $T_w = 383 \text{ K}$  at  $t = 352 \mu\text{s}$ .

## EXTERNAL FLOW

Because of the large injection pressure, the velocity of the fuel at the exit of the orifice reaches values of the order of 600 m/s (a supersonic velocity in the gas phase, but less than half the speed of sound for dodecane). We note that the shape of the tip of the jet that emerges from the injector is far from the regular shape (often a cylinder terminated by a half sphere) that is often assumed as the initial condition of injection simulations. The irregular shape of the jet is due to the non-uniform push of the liquid into the sac and is accentuated by the asymmetry of the geometry that was purposely introduced. Later stages of the simulation suggest that the interaction with the gas phase is also affected by the initial jet structure: despite the velocity of the jet being significantly above the speed of sound of air at those conditions, once the fuel exits the injector the compression of the gas is not uniform and does not lead to the formation a sustained shock ahead of the jet. In fact, the bulk of the jet seems to be preceded by a group of relatively large droplets and ligaments traveling together (see Figure 9), rather than as the mushroom-shaped front tip that appears in other studies (for instance, Shinjo, and Umemura, 2011).

The ROI and ROM are evaluated from the orifice exit cross-section as a function of time and plotted in Figure 10. The time origin corresponds to the appearance of the jet outside of the orifice. Two sets of measurements are available from Sandia and CMT-motores térmicos for similar injection conditions, and both show a slower flow rate increase with time. The initial peak from the simulation displayed in Figure 10 can be explained in terms of the extra liquid volume contained in the sac before the injection cycle begins. It is also possible that the momentum of residual gas expelled from the sac facilitates for a brief time interval the ejection of liquid. Overall, it is at present uncertain whether the overshoot in the CMT and Sandia measurements (observable between 20 and 40  $\mu\text{s}$  in Figure 10) is real (Pickett et al., 2013). In fact, the ECN recommends using a “Virtual Injection Rate Generator” (refer to the CMT website): these model values are plotted as a dashed line in Figure 10.

Once the needle is completely unseated, the expected mass flow rate is 2.62 g/s and the corresponding momentum flux is 1.52 N. After 35  $\mu\text{s}$  from the appearance of the jet, it is evident that these values are not yet met by our calculation. Further analysis is necessary to assess what fraction of the discrepancy could be attributed to insufficient resolution (or modelling) of the boundary layer in the orifice.

Finally, in Figure 11 the penetration of the jet emerging from the injector is compared to the values obtained from radiographic measurements carried out at Argonne (the field of view of the spray rig was limited to the first 7 millimetres of the jet). The symbols in the plot correspond to the ensemble average of

several injections and depend on an assigned threshold for the liquid mass. Conversely, in the simulation the penetration is measured as the distance from the injector's end of the furthest point of the contiguous jet. This criterion becomes increasingly blurry, however, as the pictures in Figure 9 suggest. Within these limits, the penetration of the simulated fuel jet appears acceptable.

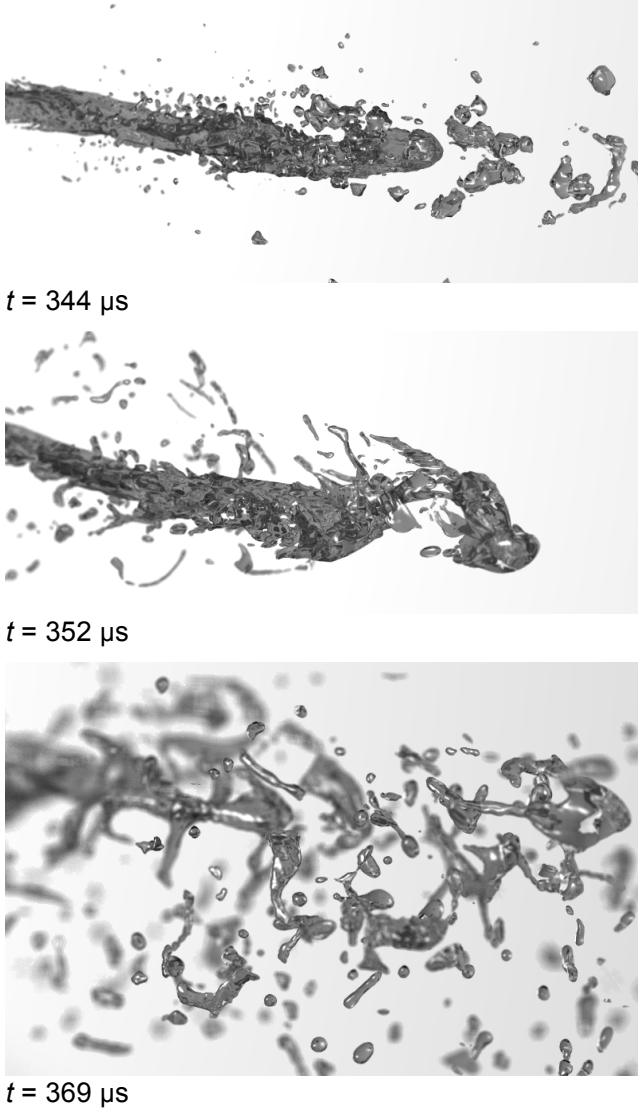


**Figure 9. Ray-traced snapshot sequence obtained by following the moving jet tip.**

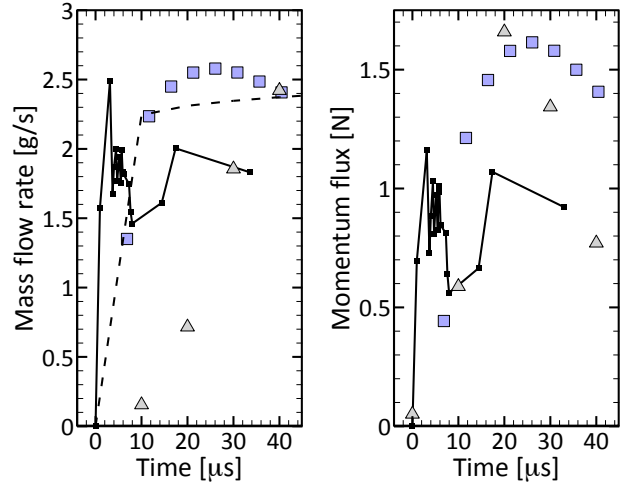


**Figure 10. Rate of injection (left) and rate of momentum (right) from the adiabatic-wall simulation (continuous line) compared with measurements from Sandia (squares) and CMT (triangles). The dashed line is the mass flow rate model proposed by ECN.**

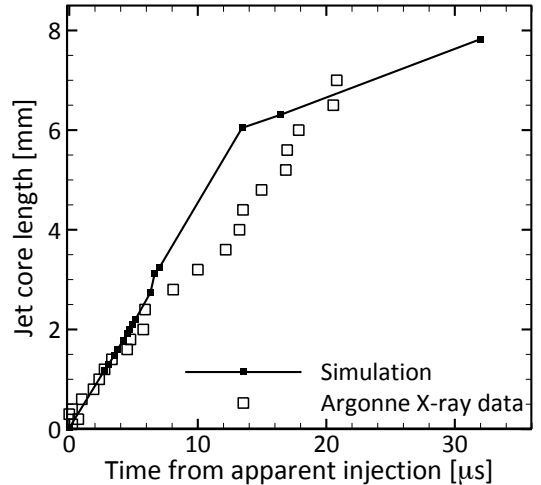


**Figure 11. Fuel jet penetration compared with experimental data from the adiabatic wall simulation.**

## CONCLUSIONS

We have examined the early transient of needle unseating, corresponding to the first 370  $\mu$ s from activation. Of these, the last 35  $\mu$ s concern the exit of the fuel from the injector and the formation of a spray. The calculation demonstrates the ease of the proposed methodology for dealing with moving boundaries and for including compressibility effects of the liquid phase.

- At the onset of needle lifting, a small amount of gas is sucked into the sac due to interference between needle tip and injector walls.
- This gas and any residual amount in the sac are ejected very rapidly as soon as the needle is activated,

exhibiting the characteristics of an under-expanded jet immediately outside the orifice.

- At adiabatic wall conditions, the fuel temperature at the orifice exit in this early phase of injection remains within a few degrees Kelvin from the reservoir temperature of 343 K. The exit temperature in the isothermal calculation is approximately 15 K larger.
- In both cases the density variation of the liquid fuel is quite substantial: from 790 kg/m<sup>3</sup> under compression upstream of the needle gap to less than 720 kg/m<sup>3</sup> at the exit of the injector.
- The calculated rate of injection and momentum are smaller than predicted by models based on the injection pressure and an assigned discharge rate. This result requires further investigation.
- Due to the non-uniform filling of the sac, the liquid exits the jet without causing a coherent compression of the gas. For several orifice diameters downstream, we observe that the liquid moves faster than the speed of sound in the gas phase but without forming a leading shock.

In closing, we note that the Reynolds numbers that can actually be resolved in the simulation are quite small. Moreover, the embedded boundary method does not allow for efficient grid spacing near the walls, as a body-fitted approach would, so that correctly capturing the boundary layer thickness remains a challenge. The use of wall functions developed for cut-cell methods might mitigate this issue. Looking forward, the continuation of the present set of simulations will have to contend with the fact that the processes of injection and spray formation is a formidably “stiff” problem, where the stable simulation time step is six orders of magnitude smaller than the injection cycle period.

## ACKNOWLEDGMENTS

Support by Sandia National Laboratories' LDRD (Laboratory Directed Research and Development) is gratefully acknowledged. Sandia National Laboratories is a multi-program laboratory managed and operated by Sandia Corporation, a wholly owned subsidiary of Lockheed Martin Corporation, for the U.S. Department of Energy's National Nuclear Security Administration under contract DE-AC04-94AL85000.

## REFERENCES

1. Arienti, M. and Sussman, M., "An Embedded Level Set Method for Sharp-Interface Multiphase Simulations of Diesel Injectors." *Int. J. of Multiphase Flow* 59: 1-14 (2014).
2. Bode, M., Diewald, F., Broll, D., Heyse, J., le Chenadec, V., and Pitsch, H., "Influence of the Injector Geometry on Primary Breakup in Diesel Injector Systems," *SAE Technical Paper* 2014-01-1427, 2014.
3. Caudwell, D.R., Trusler, J.P.M., Vesovic, V. and Wakeham, W.A., "The Viscosity and Density of n-Dodecane and n-Octadecane at Pressures up to 200 MPa and Temperatures up to 473 K." *International Journal of Thermophysics*, Vol. 25, No. 5, 2004.
4. CCSE 2012. <https://ccse.lbl.gov/BoxLib/index.html>
5. CMT "Virtual Injection Rate Generator" [www.cmt.upv.es/ECN09.aspx](http://www.cmt.upv.es/ECN09.aspx)
6. ECN 2013. <http://www.sandia.gov/ecn/cvdata/targetCondition/injectorNozGeom.php>
7. ECN2 Proceedings, Jan. 2014. <http://www.sandia.gov/ecn/workshop/ECN2.php>
8. Jemison, M., Loch, E., Sussman, M., Shashkov, M., Arienti, M., Ohta, M. and Wang, Y. "A Coupled Level Set-Moment of Fluid Method for Incompressible Two-Phase Flows." *J. of Scientific Computing*, pp. 54:454-491, 2013.
9. Jemison, M., Sussman, M., and Arienti, M., "Compressible, Multi-Phase Semi-Implicit Method with Moment of Fluid Interface Representation." *J. of Computational Physics*, 279, 182-217 (2014).
10. Kadioglu, S. Y. and Sussman, M., 2008. "Adaptive Solution Techniques for Simulating Underwater Explosions and Implosions." *J. of Comp. Phys.* 227:2083-2104.
11. Khasanshin, T. S., Shchamialiou, A. P., and Poddubskij, O. G., "Thermodynamic Properties of Heavy n-Alkanes in the Liquid State: n-Dodecane." *International Journal of Thermophysics*, Vol. 24, No. 5, 2003.
12. Kastengren, A. L., Tilocco, F. Z., Powell, C. F. Manin, J., Pickett, L. M., Payri, R., and Bazyn, T. (2012) "Engine Combustion Network (ECN): Measurements of Nozzle Diameter and Hydraulic Behavior of Diesel Sprays." *Atomization and Sprays*, 19(11): 1031-1044.
13. Padilla-Victoria, H., Iglesias-Silva, G. A., Ramos-Estrada, M., Hall K. R., 2013. "A correlation to predict speed of sound in liquids: 1. n-Alkanes ( $\geq C_5$ ) and their mixtures at high pressures." *Fluid Phase Equilibria* 338 119-127.
14. Pickett, L., Manin, J., Payri, R., Bardi, M., and Gimeno, J., "Transient Rate of Injection Effects on Spray Development." *SAE Technical Paper* 2013-24-0001, 2013.
15. Pickett, L., Manin, J., Kastengren, A., and Powell, C., "Comparison of Near-Field Structure and Growth of a Diesel Spray Using Light-Based Optical Microscopy and X-Ray Radiography," *SAE Int. J. Engines* 7(2): 1044-1053, 2014.
16. Pilliod, J., Puckett, E.: Second-order accurate volume-of-fluid algorithms for tracking material interfaces. *J. Computational Phys.* 199(2), 465–502 (2004).
17. Shinjo, J. and Umemura, A. (2011). "Detailed simulation of primary atomization mechanisms in Diesel jet sprays (isolated identification of liquid jet tip effects)." *Proceedings of the Combustion Institute* 33 2089-2097.
18. Sussman, M. and Ohta, M., 2009. A stable and efficient method for treating surface tension. *SIAM J. Sci. Comput.* 31, 2447–2471.

19. Xue, Q., Som, S., Battistoni, M., Longman, D. E.  
Zhao, H., Senecal, P. K. and Pomraning, E.  
"Three-dimensional Simulations of the Transient  
Internal Flow in a Diesel Injector: Effects of  
Needle Movement". In ILASS Americas, 25th

Annual Conference on Liquid Atomization and  
Spray Systems, Pittsburgh, PA, May 2013.

